

Effects of polydispersity on the order-disorder transition of diblock copolymer melts

T.M. Beardsley^a and M.W. Matsen^b

Department of Mathematics, University of Reading, Whiteknights, Reading RG6 6AX, UK

Received 6 August 2008

Published online: 30 October 2008 – © EDP Sciences / Società Italiana di Fisica / Springer-Verlag 2008

Abstract. The effect of polydispersity on an AB diblock copolymer melt is investigated using lattice-based Monte Carlo simulations. We consider melts of symmetric composition, where the B blocks are monodisperse and the A blocks are polydisperse with a Schultz-Zimm distribution. In agreement with experiment and self-consistent field theory (SCFT), we find that polydispersity causes a significant increase in domain size. It also induces a transition from flat to curved interfaces, with the polydisperse blocks residing on the inside of the interfacial curvature. Most importantly, the simulations show a relatively small shift in the order-disorder transition (ODT) in agreement with experiment, whereas SCFT incorrectly predicts a sizable shift towards higher temperatures.

PACS. 82.35.Jk Copolymers, phase transitions, structure – 61.46.-w Structure of nanoscale materials

1 Introduction

Block copolymer melts have received considerable attention in recent years due to their intriguing phase behavior and varied applications. Although chemists can readily synthesize a wide range of architectures, most of the research focuses on the simple monodisperse AB diblock copolymer system. In this ideal case, every polymer is identical with N_A A-segments and N_B B-segments, giving a total degree of polymerization of $N = N_A + N_B$ and an A-segment composition of $f = N_A/N$. When the interaction between unlike segments becomes sufficiently unfavorable (as measured by the Flory-Huggins χ parameter), the copolymers self-assemble into periodically ordered structures with nanometer-sized domains. The equilibrium phase diagram contains the classical lamellar (L), cylindrical (C), and spherical (S) phases, as well as a complex gyroid (G) phase [1]. Experiments often observe another complex perforated-lamellar (PL) phase [2], but it is only metastable and eventually converts to gyroid given sufficient time [3]. More recently, a third complex phase with Fddd symmetry has been reported [4], which appears to be stable but only in a very small region of the phase diagram. In remarkable agreement, self-consistent field theory (SCFT) predicts a phase diagram with both G [5] and Fddd [6] as stable phases, while it finds PL to be nearly stable [5]. The main inaccuracy of SCFT occurs at

weak segregations, where it predicts that the three classical phases converge to a common critical point. This is rectified when fluctuations are taken into account, either by correcting the mean-field approximation of SCFT [7] or by performing simulations [8,9]. Not everything is yet perfectly consistent as the fluctuation corrections also eliminate the Fddd region [10], but nevertheless the agreement between theory and experiment is still very good.

There has been a long-held opinion that the formation of well-ordered morphologies requires block copolymers with narrow molecular weight distributions (MWDs) [11]. Only recently, have experimentalists started to realize that this is not necessarily so [11,12]. The implications are highly significant, because this means that the block copolymer molecules could be synthesized by less costly techniques. To take full advantage of this, it is important to understand how polydispersity affects block copolymer phase behavior. There has been considerable progress already, but many questions still remain.

The model system for most of the experimental [13–16] and theoretical [17–20] studies involves diblock copolymers with a polydisperse A-block and a monodisperse B-block. The degree of polydispersity in the A-block is specified by the polydispersity index, $PDI_A \equiv (N_A)_w / (N_A)_n$, which increases from one as the MWD becomes broader. It is already well established that polydispersity reduces the entropic stretching energy of a domain, since polydisperse blocks are able to fill space more efficiently [17]. As a consequence, theory predicts the domain size to increase with polydispersity [17–19], and experiments have

^a e-mail: t.m.beardsley@reading.ac.uk

^b e-mail: m.w.matsen@reading.ac.uk

confirmed this [13, 14, 21]. Another consequence is that the internal interfaces tend to curve towards the polydisperse domains in order to relieve the stretching energy of the monodisperse domains [18–20], and this too has been confirmed by experiment [14–16]. Because polydisperse melts are actually multi-component systems, two-phase coexistence regions will emerge between all the single-phase regions. Theory predicts that some of these coexistence regions become particularly large consuming much of the complex phase region [20], and there are a number of experiments supporting this [12, 13, 21].

There is one notable inconsistency between theory and experiment with regards to the effect of polydispersity on the order-disorder transition (ODT). SCFT predicts that the position of the ODT, $(\chi N)_{ODT}$, is lowered with respect to monodisperse melts at all compositions [18–20]. On the other hand, recent experiments by Lynd and Hillmyer [15] on two different systems show that, while $(\chi N)_{ODT}$ decreases when the minority component is polydisperse, it actually increases when the majority component is polydisperse. The natural explanation is that polydispersity enhances fluctuation effects, particularly when the majority component is polydisperse. Although the standard Fredrickson-Helfand correction for fluctuations [7] has not yet been applied to this system, it has been applied to diblocks in which both blocks are equally polydisperse [22]. That study found that, if anything, polydispersity reduces the effect of fluctuations. Since then, however, there have been some concerns raised regarding the validity of the Fredrickson-Helfand correction, and more rigorous treatments are now under development [23]. In light of this, we turn to Monte Carlo simulations to investigate this inconsistency between the Lynd-Hillmyer experiments [15] and the SCFT prediction for the ODT [18–20].

2 Monte Carlo algorithm

Our simulations use a lattice-based Monte Carlo algorithm introduced by Vassiliev and Matsen [24] for melts of monodisperse diblock copolymers. Since it has been previously reported, we simply summarize its main features and describe the alterations required to handle polydisperse MWDs. The model consists of n diblock copolymers each with a B-block of exactly N_B monomers. Of these molecules, n_{N_A} have an A-block of N_A monomers, such that the number-averaged polymerization is $(N_A)_n = \sum N_A n_{N_A} / n$. As before, the polymer chains are placed on an artificial lattice with periodic boundary conditions, with no more than one monomer per lattice site, and with each pair of bonded monomers occupying nearest-neighbor sites. In order to minimize the effects of the lattice, we employ a close-packed lattice with a coordination number of $z = 12$. It is obtained by taking an $L \times L \times L$ simple cubic lattice with a lattice constant of d and deleting every second site, producing an fcc lattice with $V = L^3/2$ sites and a nearest-neighbor distance of $b = \sqrt{2}d$. To allow room for the polymers to move, the fcc lattice is only partially filled to a copolymer occupancy of $\phi_c \equiv nN/V \approx 0.8$. The only

molecular interactions are between neighboring A and B monomers, with an interaction strength of ϵ_{AB} from which we define the dimensionless Flory-Huggins parameter,

$$\chi \equiv \frac{z\epsilon_{AB}}{k_B T}. \quad (1)$$

Although analogous to the χ parameter defined for the continuum Gaussian chain model used in SCFT, this particular definition is specific to lattice models.

For a given $(N_A)_n$, N_B , PDI_A and L , our simulations begin with a cooling run starting in the disordered phase at $\chi = 0$ and stepping up in small increments until the system forms a well-ordered morphology. This is then followed by a heating run back into the disordered state. After every increment in χ , the system is equilibrated with 2×10^4 Monte Carlo steps (MCS) per monomer. Four types of moves are permitted: the slithering snake, chain reversal, crankshaft and block exchange, as described in reference [24]. Once the relaxation period is finished, a further 8×10^4 MCS per monomer are performed, during which various thermodynamic averages are evaluated by sampling one configuration every 40 MCS per monomer. For our selection of system sizes, each step in χ requires from one to three days of CPU time on an AMD Opteron 2.6 GHz processor.

The simplest quantity to evaluate is the internal energy, $U = \epsilon_{AB} \langle n_{AB} \rangle$, where n_{AB} is the total number of A/B contacts and the angle brackets denote Monte Carlo averages. The heat capacity is also easily calculated using $C_V = (\epsilon_{AB}^2 \langle n_{AB}^2 \rangle - U^2) / k_B T^2$. To quantify the domain structure of the melt, we examine the correlation function,

$$G_{ij} = \langle \sigma_i \sigma_j \rangle - \langle \sigma_i \rangle^2, \quad (2)$$

where $\sigma_i = 1, 0$ or -1 if the i -th lattice site is occupied by an A-monomer, a vacancy or a B-monomer, respectively. From the correlation function, we obtain the structure function

$$S(\mathbf{q}) = \frac{1}{V} \sum_{ij} G_{ij} \exp[i\mathbf{q} \cdot (\mathbf{r}_i - \mathbf{r}_j)], \quad (3)$$

which corresponds to the pattern observed in small-angle scattering experiments.

Many past studies [25] have struggled to locate the ODT despite the fact that the transition must be first order, and it will prove to be even more difficult for polydisperse melts. All the usual thermodynamic quantities should exhibit discontinuities at the ODT, but unfortunately they are generally so small as to be obscured by the statistical noise. Hence, we are in need of an *order parameter* with a more pronounced sensitivity to the ODT. We are not concerned whether or not it has a simple physical interpretation, but it should ideally be zero (or at least very small) in the disordered phase and relatively large in the ordered phase. References [8] and [24] have recently demonstrated that

$$\psi = \frac{1}{V^2} \sum_{i \neq j} G_{ij}^2 \quad (4)$$

meets these requirements. The disordered phase results in a small value of ψ because the double summation only scales as V due to the limited range of G_{ij} , whereas the summation scales as V^2 once the morphology acquires long-range order.

3 Polydispersity distribution

The behavior of polydisperse melts depends to some degree on the detailed shape of the distribution [26], but we ignore this issue for now and simply use the standard Schultz-Zimm distribution [27],

$$p(N_A) = \frac{k^k N_A^{k-1}}{(N_A)_n^k \Gamma(k)} \exp\left(-\frac{k N_A}{(N_A)_n}\right), \quad (5)$$

where $\text{PDI}_A \equiv (N_A)_w / (N_A)_n = (k+1)/k$. However, this is a continuous distribution, whereas we require a discrete distribution, $\{n_{N_A}\}$, of

$$n = \sum_{N_A} n_{N_A} \quad (6)$$

chains with a specified number-averaged length of

$$(N_A)_n = \frac{1}{n} \sum_{N_A} N_A n_{N_A}. \quad (7)$$

This is achieved by defining the probability, p_{N_A} , of an A-block to have N_A segments as the integral of $p(N_A)$ from $N_A - 0.5$ to $N_A + 0.5$, except for $N_A = 0$ in which case the integral starts from zero. Then we select the number of A-blocks with N_A segments to be $n_{N_A} \approx np_{N_A}$, keeping in mind that this must also be an integer.

To obtain a suitable set of integers, $\{n_{N_A}\}$, for $N_A = 0$ to some reasonable large value, we begin by rounding np_{N_A} down to the nearest integer. Naturally this will result in too few chains by an amount m_c as well as too few segments by an amount m_s . This is corrected for by incrementing n_{N_A} by one for $N_A = \text{int}(m_s/m_c - (m_c - 1)/2)$ to $\text{int}(m_s/m_c + (m_c - 1)/2)$. If necessary, a final correction is applied by adding or removing one chain of the appropriate molecular weight so that equations (6) and (7) are satisfied.

To optimize the distribution further, we minimize

$$\Omega(\{n_{N_A}\}) \equiv \sum_{N_A} [n_{N_A} - np_{N_A}]^2 + \lambda \left[n(N_A)_n^2 \text{PDI}_A - \sum_{N_A} N_A^2 n_{N_A} \right]^2, \quad (8)$$

subject to the constraints of equations (6) and (7). The first summation acts to match n_{N_A} to np_{N_A} , while the second term acts to match the actual polydispersity to the target value of PDI_A . The parameter, λ , which dictates the relative importance of the two contributions, is selected to be about 10^{-7} . The minimization is done by attempting

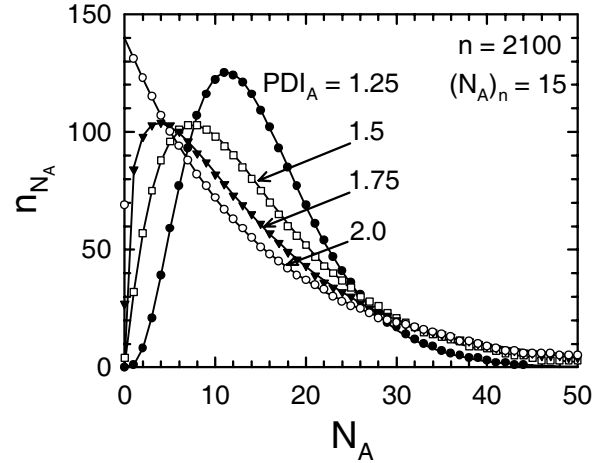


Fig. 1. Discrete distribution, $\{n_{N_A}\}$, calculated for a system of $n = 2100$ diblocks with an average A-block polymerization of $(N_A)_n = 15$ and various A-block polydispersities, PDI_A . The solid curves compare $np(N_A)$ from the continuous Schultz-Zimm distribution in equation (5).

to remove an A-segment from a chain with $N_A = j$ and adding it to a chain with $N_A = k$, which corresponds to

$$\begin{aligned} n_j &\rightarrow n_j - 1, \\ n_{j-1} &\rightarrow n_{j-1} + 1, \\ n_k &\rightarrow n_k - 1, \\ n_{k+1} &\rightarrow n_{k+1} + 1. \end{aligned}$$

We continue this process until there are no remaining moves that reduce $\Omega(\{n_{N_A}\})$.

Figure 1 compares the resulting discrete distribution, $\{n_{N_A}\}$, to the continuous distribution, $np(N_A)$, obtained from equation (5), for $n = 2100$ chains with an average A-block polymerization of $(N_A)_n = 15$. These results are used for simulation boxes of size $L = 54$. The only discernible difference between the discrete and continuous distributions is in the large- N_A tails. In this example, the actual polydispersity indices are $\text{PDI}_A = 1.241, 1.486, 1.736$ and 1.980 as compared to the target values of $1.25, 1.5, 1.75$ and 2.0 , respectively. Although the agreement is slightly reduced for smaller n (*i.e.*, smaller simulation boxes), we always manage to keep PDI_A within 2% of its intended value.

4 Results

This section presents results from a series of simulations on AB diblock copolymer melts varying the degree of A-block polydispersity over the values, $\text{PDI}_A = 1.0, 1.25, 1.50, 1.75$ and 2.0 . All the simulations are performed with diblocks of average polymerization, $N \equiv (N_A)_n + N_B = 30$, and average composition, $f \equiv (N_A)_n / N = 0.5$. To ensure that the results are not significantly affected by the finite size of the simulation box, the runs are repeated for three different system sizes, $L = 44, 54$, and 64 , which correspond to melts of $n = 1136, 2100$, and 3495 polymers, respectively.

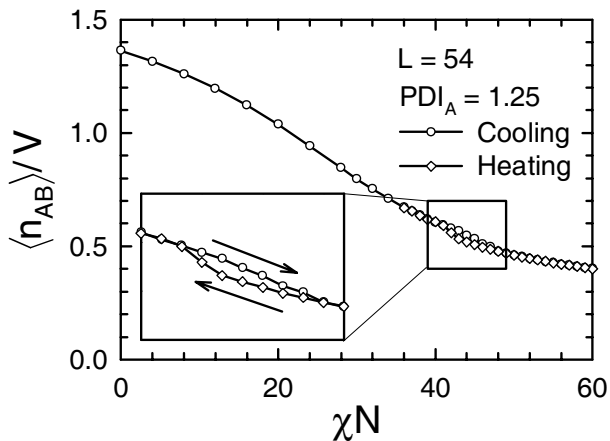


Fig. 2. Average number of A/B contacts, $\langle n_{AB} \rangle$, as the segregation, χN , is cycled during a simulation involving diblocks with an A-block polydispersity of $PDI_A = 1.25$ in a simulation box of size $L = 54$. The inset magnifies a hysteresis loop signifying the existence of the ODT.

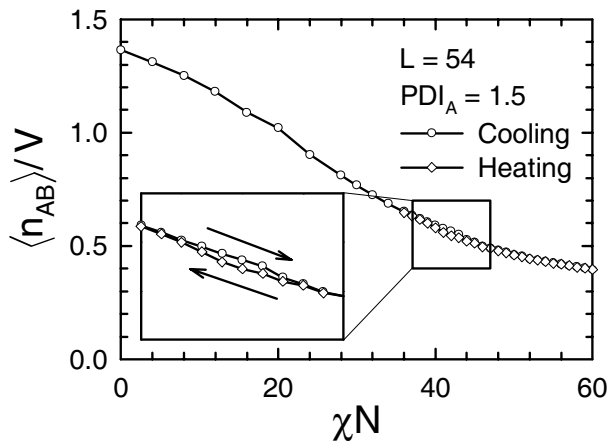


Fig. 3. Analogous plot to that of Figure 2, but for a larger A-block polydispersity of $PDI_A = 1.5$.

4.1 Energy

Figure 2 starts by examining the average number of unfavorable A/B contacts, $\langle n_{AB} \rangle$, which is directly proportional to the internal energy, U . As χN increases from zero, the unlike segments begin to form separate domains, causing a gradual decrease in the number of A/B contacts. At the ODT, however, the microstructure reduces its interfacial area by developing a regular periodic morphology, which causes an abrupt decrease in $\langle n_{AB} \rangle$. This discontinuity can be used to locate the ODT [24,28], but it tends to be very small and difficult to discern amongst the statistical noise. The best way to detect it is to produce a hysteresis loop by reversing the direction of χN , as illustrated in the inset of Figure 2 for diblocks with an A-block polydispersity of $PDI_A = 1.25$. Unfortunately, the magnitude of the hysteresis becomes progressively smaller as the polydispersity increases. It is barely visible in Figure 3 for $PDI_A = 1.5$, and is unobservable for the higher polydispersities.

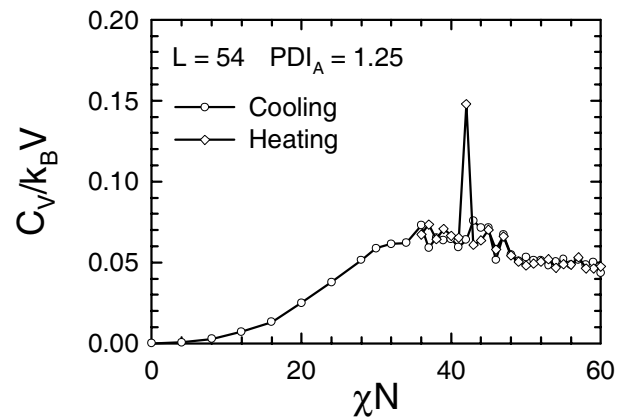


Fig. 4. Heat capacity, C_V , as the segregation, χN , is cycled during a simulation involving diblocks with an A-block polydispersity of $PDI_A = 1.25$ on a lattice of size $L = 54$.

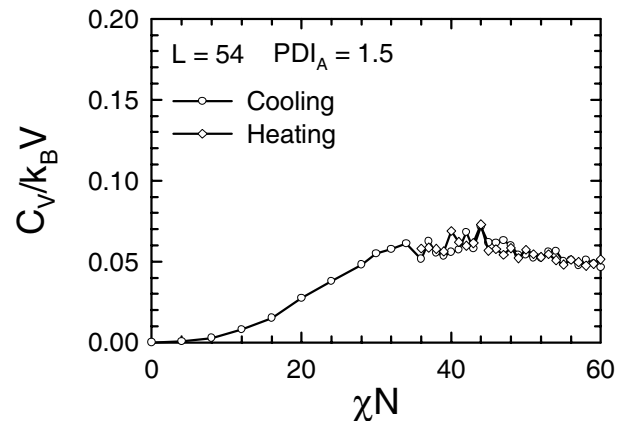


Fig. 5. Analogous plot to that of Figure 4, but for a larger A-block polydispersity of $PDI_A = 1.5$.

4.2 Specific-heat capacity

Another way of detecting the ODT is with the heat capacity, C_V , which should, in principle, exhibit a spike when there is a discontinuity in the internal energy [24,28]. It is shown in Figures 4 and 5 for heating and cooling runs for $PDI_A = 1.25$ and 1.5, respectively. For the lower polydispersity, a spike is indeed observed in the heating run, but not when the system is cooled. In this case, we attribute the absence of a spike to the phase transition occurring within the equilibration period of the simulation, such that the large energy fluctuations are not captured by the subsequent statistical averaging. For $PDI_A = 1.5$ as well as for the higher polydispersities, there are no significant spikes in the heat capacity. This complete absence of identifiable peaks is presumably a result of the reduced discontinuity in the internal energy, as evident in Figures 2 and 3. Thus C_V also fails to be an adequate indicator of the ODT for polydisperse melts.

4.3 Order parameter

We now turn to the order parameter, ψ , defined in equation (4), because it is expected to exhibit a much stronger

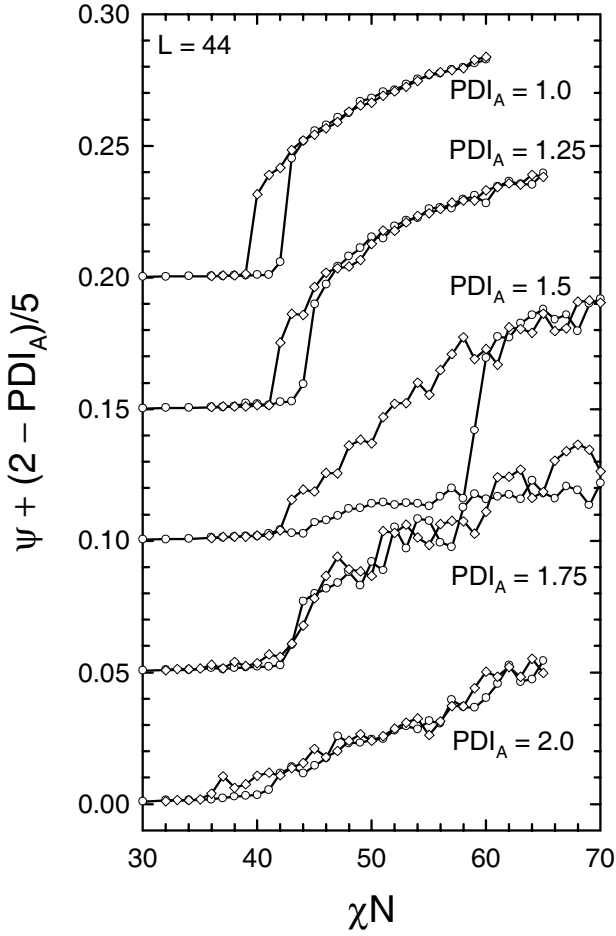


Fig. 6. Order parameter for cooling (\circ) and heating (\diamond) runs for polydispersity indices, $\text{PDI}_A = 1.0, 1.25, 1.5, 1.75$ and 2.0 , obtained from diblocks of average polymerization $N = 30$ in a simulation box of size $L = 44$. For the purpose of clarity, the curves are shifted vertically by 0.05 following each increment in PDI_A .

hysteresis [8, 24]. Figure 6 plots ψ for a series of cooling and heating runs, using a relatively small simulation box of $L = 44$. Note that the results for different PDI_A values are shifted along the vertical axis for the purpose of clarity. In each case, ψ is essentially zero in the disordered phase and is reasonably positive in the ordered phase; this time the ODT is evident even for the highest polydispersity. For $\text{PDI}_A = 1.0$ and 1.25 , the hysteresis loop is well pronounced and relatively narrow, locating the ODT at $\chi N \approx 41$ and 43 , respectively. For $\text{PDI}_A = 1.5$, the system does not fully order during the cooling run until $\chi N = 58$, but it disorders at a typical $\chi N = 42$ upon heating. The explanation for the unusually large hysteresis will become evident when we examine the system configurations in the next section; the actual ODT is undoubtedly near the low- χN end of the hysteresis loop. For the highest polydispersities of $\text{PDI}_A = 1.75$ and 2.0 , the hysteresis is almost nonexistent, but nevertheless an ODT is still evident at $\chi N \approx 40$.

It is well known that simulations involving periodically ordered phases are prone to complicated finite-size

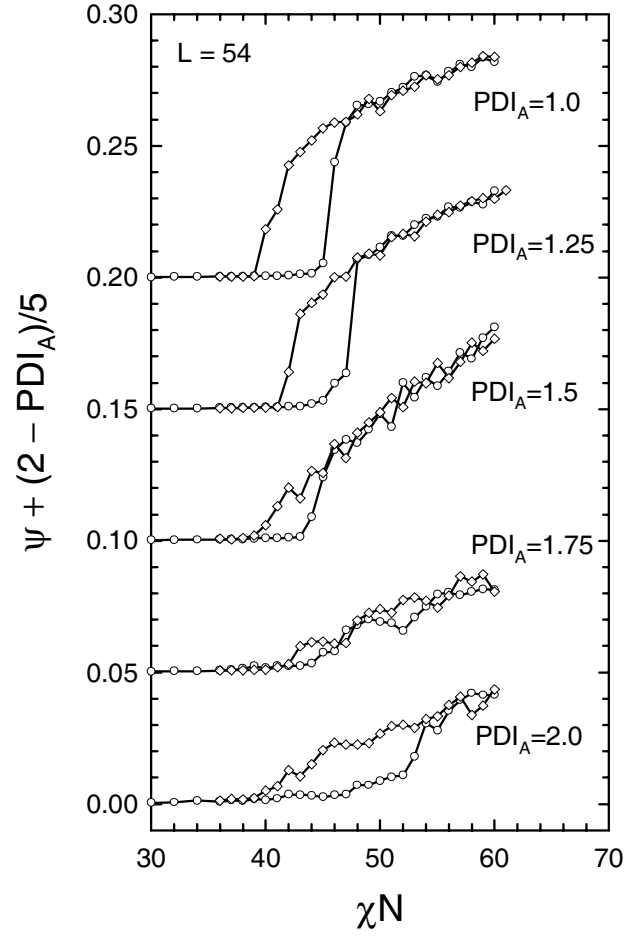


Fig. 7. Analogous plot to that of Figure 6, but for runs using a larger simulation box of size $L = 54$.

effects [25]. On one hand, small boxes tend to favor ordered phases, because of the self-correlation created by the periodic boundary conditions. On the other hand, small boxes severely restrict the allowed periodicities, which prevent to varying degrees the ordered phases from acquiring their preferred domain size. Therefore, we provide additional simulation results in Figures 7 and 8 for larger boxes of $L = 54$ and 64 , respectively. Fortunately, the finite-size effects are not too severe as evident from the fact that the hysteresis loops are reasonably similar; the values of χN at the upper and lower bounds are summarized in Table 1 for our three different system sizes.

Naturally the size and position of the hysteresis loops are significantly affected by random chance. To demonstrate this point, we have repeated the simulations for $L = 54$, and have included the limits of their hysteresis loops in Table 1 in square brackets. The lower limits are consistent, but there is considerable fluctuation in the upper limits. In light of this, it is difficult to pick out any systematic changes with system size, L . Nevertheless, it seems that the upper bounds do generally shift to higher χN for the bigger system sizes, as expected. While ordered morphologies should disorder just as easily when the system size is increased, it should normally take longer

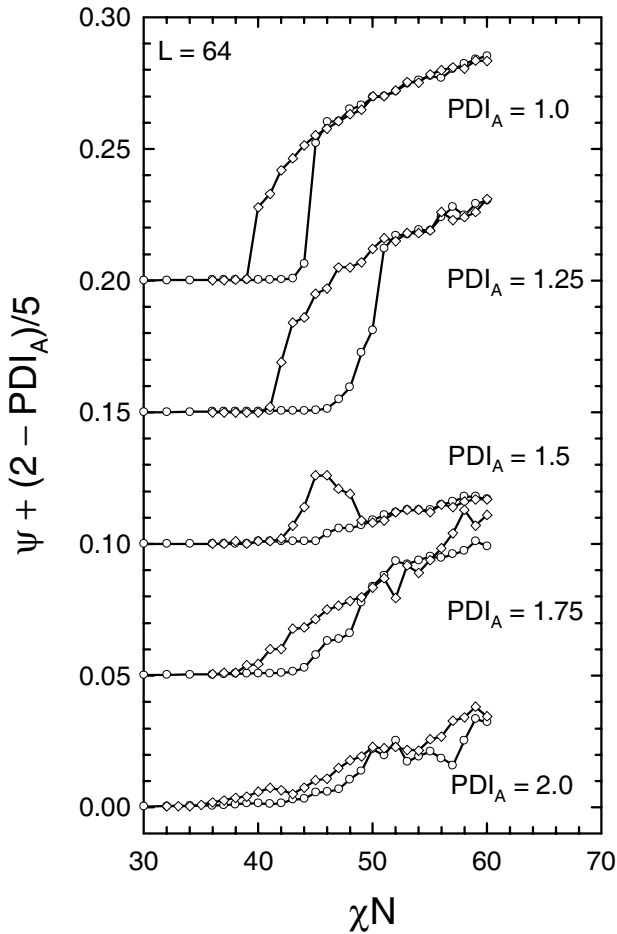


Fig. 8. Analogous plot to that of Figure 6, but for runs using a larger simulation box of size $L = 64$.

Table 1. Upper and lower bounds of the hysteresis loops shown in Figures 6–8. For the system size of $L = 54$, the square brackets contain results for a second set of statistically independent hysteresis loops (not shown).

PDI _A	$L = 44$	$(\chi N)_{ODT}$		$L = 64$
		$L = 44$	$L = 54$	
1.0	39-43	39-46 [39-54]	39-45	
1.25	41-45	41-48 [40-45]	41-51	
1.5	42-59	39-45 [39-48]	42-48	
1.75	40-44	42-47 [42-53]	39-49	
2.0	36-42	39-54 [39-42]	36-50	

for disordered melts to self-assemble in a single coherent structure when there are more molecules involved.

4.4 Disordered-state structure function

Here we investigate the disordered state by examining its structure function, $S(q)$, a quantity that can be calculated analytically from mean-field theory (see App. A). It is, in principle, an isotropic function depending on just the magnitude of the wave vector, \mathbf{q} , which takes on all

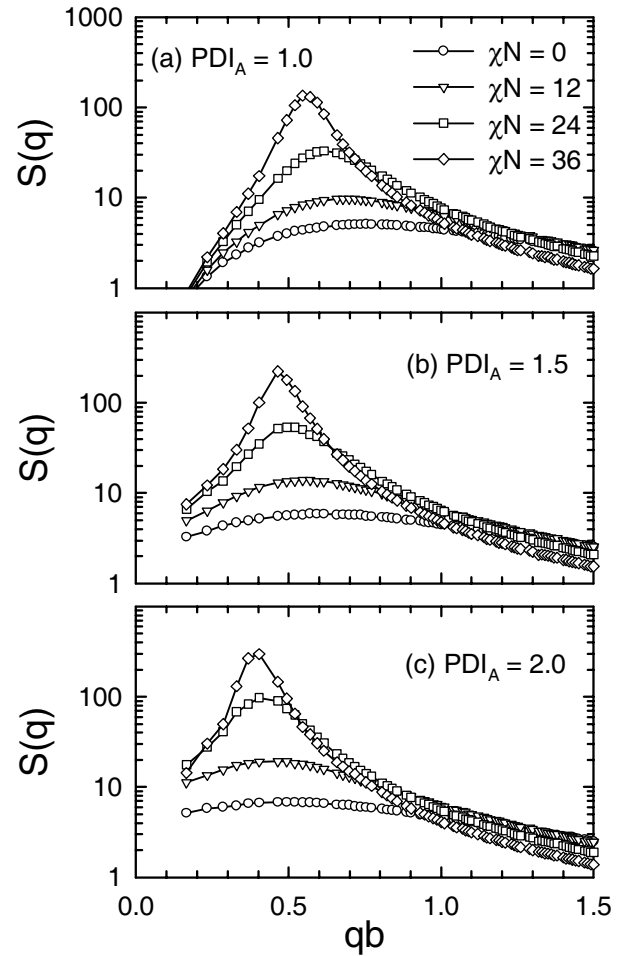


Fig. 9. Structure function, $S(q)$, plotted for a series of segregations, χN , within the disordered phase for polydispersities of (a) $PDI_A = 1.0$, (b) 1.5 and (c) 2.0. The results are from a simulation box of size $L = 54$.

values in three-dimensional reciprocal space. In our Monte Carlo study, however, the finite size of the simulation box restricts the allowed wave vectors to $\mathbf{q} = 2\pi(h, k, l)/Ld$, where h, k , and $l = 0, 1, 2, \dots, L - 1$. Furthermore, there will be some anisotropy from the cubic shape of the simulation box, but this turns out to be negligible. Therefore, it still makes sense to plot $S(q)$ as a function of $q \equiv |\mathbf{q}|$, averaging over all wave vectors of the same magnitude. The resulting structure function is displayed in Figure 9 for a series of χN values below $(\chi N)_{ODT}$ and for polydispersities of $PDI_A = 1.0, 1.5$ and 2.0 . We only show plots for $L = 54$, because the results from our other two system sizes are virtually indistinguishable.

As demonstrated previously [19], mean-field theory (*i.e.*, SCFT) predicts a shift in the peak, q^* , of the structure function towards smaller wave vectors with increasing PDI_A . This indicates that the characteristic domain size, $2\pi/q^*$, in the disordered phase becomes larger for polydisperse melts. The same trend is observed in Figure 9 for our Monte Carlo simulations. The peak positions at $\chi N = 36$ along with the characteristic domain sizes are listed in Table 2 for the different polydispersities. The peaks are

Table 2. Characteristic domain sizes, $2\pi/q^*$, at $\chi N = 36$ in the disordered phase for different A-block polydispersities, PDI_A , obtained from the peak, q^* , in the structure function, $S(q)$.

PDI_A	$2\pi/q^*b$		
	$L = 44$	$L = 54$	$L = 64$
1.0	11.4	11.4	11.4
1.25	12.3	12.4	12.3
1.5	13.4	13.7	13.4
1.75	14.7	14.6	14.4
2.0	16.0	15.9	15.7

estimated by fitting the discrete values of $S(q)$ (*i.e.*, the symbols) to smooth curves.

There are, however, some qualitative differences between our simulations and the SCFT predictions. First of all, SCFT predicts that q^* is independent of χ , whereas the simulations show that the peak moves towards smaller wave vectors with increasing χ . This is a well-known fluctuation effect [29] that has already been observed in simulations on monodisperse melts [24]. SCFT also predicts a significant increase in the peak as the polydispersity is increased [19], whereas the simulations do not. The divergence in the peak indicates the onset of the ODT, and so this effect just reiterates our previous finding that $(\chi N)_{ODT}$ is approximately constant in the simulations, whereas SCFT predicts a significant decrease with increasing polydispersity.

4.5 Ordered morphologies

Our study concludes by examining the ordered phases, plotted in Figures 10, 11, and 12 for the three different system sizes, $L = 44, 54,$ and 64 , respectively. Once an ordered morphology forms during the cooling run, its structure and periodicity are effectively locked in until it finally disorders during the subsequent heating run. Therefore, we only show one snapshot for each run taken at $\chi N = 60$. All the morphologies turn out to be either lamellar (L) or perforated-lamellar (PL). For clarity, the A- and B-monomers are shown separately, and the simulation boxes are rotated so that the lamellae appear edge on.

The configurations provide considerable insight into the behavior of the order parameter. For instance, it is now easy to explain the anomalous case in Figure 8 for $PDI_A = 1.5$, where there was no significant jump in the order parameter until the heating run at $\chi N = 48$. Looking at the corresponding configuration in Figure 12, we see that the ordered lamellar phase contains a defect, specifically a screw dislocation. Similarly, the large hysteresis in Figure 6 for $PDI_A = 1.5$ was also the result of a persistent defect, but one that managed to anneal out during the cooling run just before $\chi N = 60$. Clearly such events occur by random chance, and this is why there is so much statistical variation in the upper bounds of the hysteresis loops. No such issue occurs when the morphologies disorder upon heating, which explains why there is much less variation in the lower bounds.

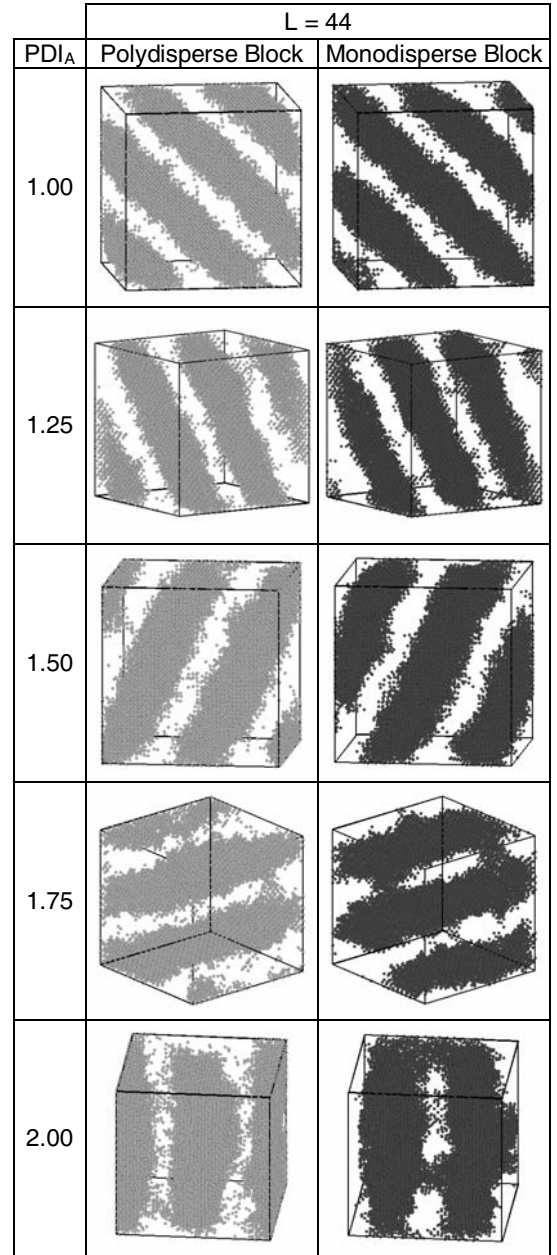


Fig. 10. Ordered morphologies for various polydispersities obtained at $\chi N = 60$ from simulations on a lattice of size $L = 44$. For clarity, the A monomers of the polydisperse blocks (grey) are shown separately from the B monomers of the monodisperse blocks (black).

It is also evident that the relatively large jumps in the order parameter at the lower A-block polydispersities coincide with the formation of simple L phases. As the polydispersity increases, the magnitude of the order parameter is reduced by the presence of small struts that pass through the polydisperse A-domains joining together adjacent monodisperse B-domains; see $PDI_A = 1.5$ for $L = 54$ and $PDI_A = 1.75$ for $L = 44$ and 64 . By following the evolution of these configurations during the simulations, we find that the struts are transient features that only last for a few thousand MCS per monomer, and thus

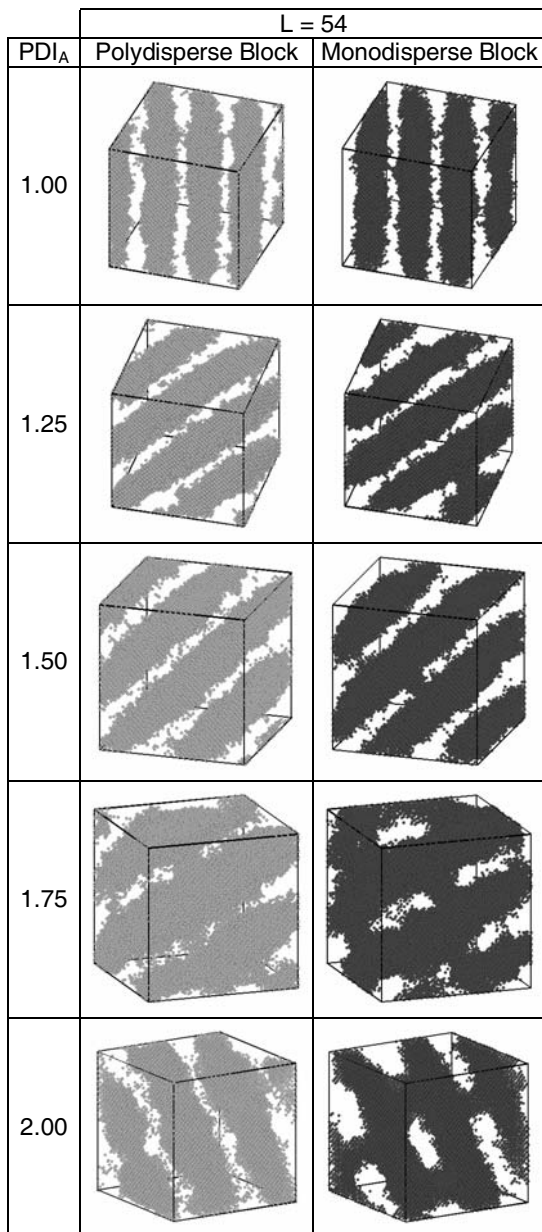


Fig. 11. Analogous plots to those of Figure 10, but for a larger system size of $L = 54$.

the symmetry is still that of a L phase. However, this behavior is a precursor for what happens at the highest polydispersity. For $PDI_A = 2.0$, the struts become much thicker and remain as permanent features; the morphology is now classified as a PL phase. This also happens at $PDI_A = 1.75$ for the intermediate system size, but we attribute this to a frustrated lamellar period as explained below.

It may seem that the lamellar orientations in Figures 10–12 are selected randomly, but this is not so. For each of the lamellar morphologies, Table 3 provides the principle wave vector and corresponding periodicity. As we can see, the orientation is selected so that the lamellar period matches reasonably well with the peak in $S(q)$ (see

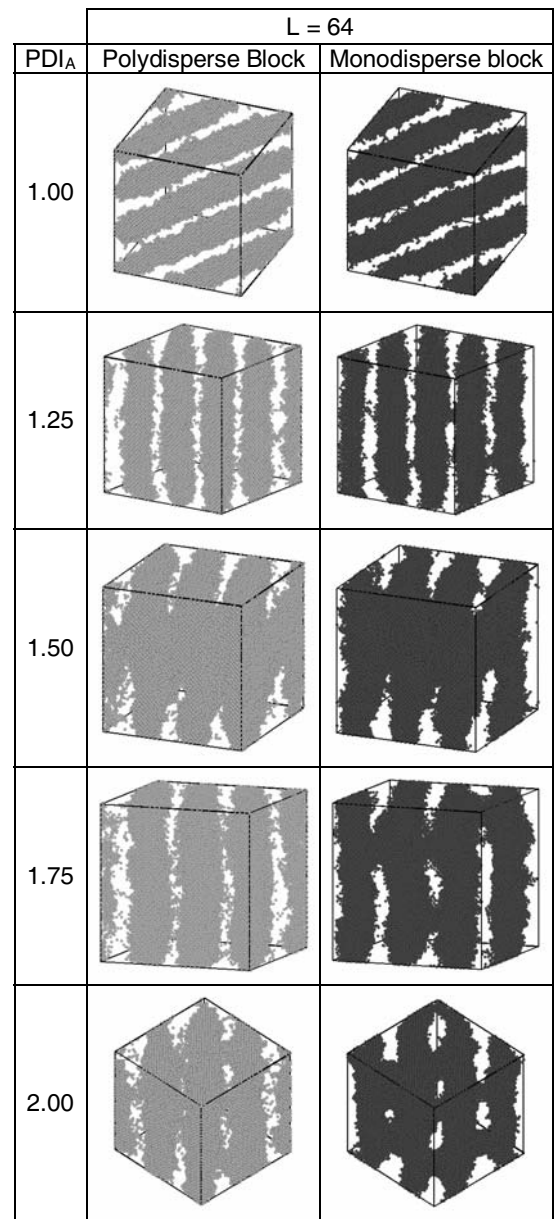


Fig. 12. Analogous plots to those of Figure 10, but for a larger system size of $L = 64$.

Table 2). Again the domain size is reasonably independent of the system size, L , and shows a clear increasing trend with polydispersity, PDI_A .

Note that the discreteness in the allowed lamellar periods can cause some frustration in the morphology. Take $PDI_A = 1.75$, for example, where $S(q)$ indicates a preferred lamellar periodicity of $D \approx 14.6b$. Unfortunately, the $L = 54$ simulation box does not allow for any periodicities between $D = 13.5b$ or $15.6b$ (corresponding to $q = 0.465/b$ and $0.403/b$, respectively). As it happened, the system opted for the larger domain spacing and we suspect that the resulting frustration was responsible for the formation of permanent perforations, which were absent for $L = 44$ and 64 .

Table 3. Components of the principal wave vector, $\mathbf{q}^* = 2\pi(h, k, l)/Ld$, and the corresponding lamellar periodicity, $D = 2\pi/q^*$, for each of the configurations in Figures 10–12. Note that the result for $\text{PDI}_A = 1.5$ and $L = 64$ was obtained at $\chi N = 48$ during the heating run.

PDI _A	$(h, k, l) D/b$		
	$L = 44$	$L = 54$	$L = 64$
1.0	(2,2,0) 11.0	(3,1,0) 12.1	(3,2,1) 12.1
1.25	(2,1,1) 12.7	(2,2,1) 12.7	(3,2,0) 12.6
1.5	(2,1,0) 13.9	(2,2,0) 13.5	(3,1,1) 13.6
1.75	(2,1,0) 13.9	(2,1,1) 15.6	(3,1,0) 14.3
2.0	(2,0,0) 15.6	(2,1,1) 15.6	(2,2,0) 16.0

Although the lamellar orientation is largely controlled by the preferred periodicity, there is nevertheless some element of random chance. This is illustrated by our second set of statistically independent runs at $L = 54$, where the lamellae for $\text{PDI}_A = 1.0$ and 1.25 both selected a $(3, 0, 0)$ wave vector corresponding to $D = 12.7b$. For the three larger values of PDI_A , however, the same orientations were selected as in Table 3, with permanent perforations forming again for $\text{PDI}_A = 1.75$ and 2.0 .

5 Discussion

The principal objective of our Monte Carlo simulations was to address the inconsistency between SCFT [20] and the experiments of Lynd and Hillmyer [15], regarding the effect of polydispersity on the location of the ODT. At symmetric composition (*i.e.*, $f = 0.5$), SCFT predicts $(\chi N)_{ODT} = 10.495, 9.72, 8.65,$ and 7.54 for $\text{PDI}_A = 1.0, 1.2, 1.5,$ and 2.0 , respectively, which represents a sizable 28% reduction. In contrast, the experiments on symmetric melts of poly(ethylene-alt-propylene)-poly(DL-lactide) diblocks found a slight increase from $(\chi N)_{ODT} = 9.63$ at $\text{PDI}_A = 1.22$ to $(\chi N)_{ODT} = 10.2$ at $\text{PDI}_A = 1.35$ followed by a small decrease to $(\chi N)_{ODT} = 9.27$ at $\text{PDI}_A = 2.0$, which seriously contradicts the SCFT prediction. Note that we do not compare the experimental results for poly(styrene)-poly(isoprene) diblocks, because Lynd and Hillmyer only examined three samples of symmetric composition covering the small range, $\text{PDI}_A = 1.21, 1.29,$ and 1.34 ; furthermore, any polydispersity effect would undoubtedly be obscured by the unusually large uncertainty in the measured $(\chi N)_{ODT}$ of the last sample.

In our simulations, the true equilibrium ODT will generally lie within the hysteresis loop, presumably close to the lower- χN limit. As we have clearly seen, the occurrence of defects can seriously delay the formation of an ordered phase, which can push the upper limit to exceptionally high values of χN . The problem is that there are relatively few configurations of the system that correspond to an ordered morphology. On the other hand, there are many configurations that conform to a disordered morphology, and consequently it is relatively easy for the system to find its way from an ordered to a disordered state. This being the case, our simulations indi-

cate that $(\chi N)_{ODT}$ hovers around 40 for the entire range of $\text{PDI}_A = 1.0$ to 2.0 . If anything, there is a slight increase in $(\chi N)_{ODT}$ up to $\text{PDI}_A = 1.5$ followed by a similar decrease in $(\chi N)_{ODT}$ as PDI_A approaches 2.0 , which is very reminiscent of the experiments. However, we should not overemphasize the agreement; these small variations in $(\chi N)_{ODT}$ are comparable to both the experimental uncertainty and our statistical noise, and furthermore the composition of the experimental samples varied between $f = 0.488$ and 0.511 . In any case, the agreement is far better than with SCFT. Note that our comparison with experiment is only concerned with relative changes in $(\chi N)_{ODT}$ and not with the absolute values, because the experiments obtained χ by fitting the ODT of monodisperse diblocks to the SCFT prediction, $(\chi N)_{ODT} = 10.495$.

The qualitative difference between our simulations and SCFT is presumably due to fluctuation effects, which shift the mean-field ODT to higher values of χN . The shift increases for shorter polymers as determined by the invariant polymerization index, $\bar{N} \equiv a^6 v^{-2} N$, where a is the statistical segment length and v is the segment volume. The size of the effect is usually estimated by the method of Fredrickson and Helfand [7]. Although no such calculation has been performed for our particular system, Burger *et al.* [22] have applied the method to diblock copolymers where both blocks are equally polydisperse. Without the correction, SCFT predicts $(\chi N)_{ODT} = 10.495, 7.340,$ and 4.895 for $\text{PDI} = 1.0, 1.4,$ and 1.8 , respectively. For polymers of $\bar{N} = 10^4$, these values are shifted to $(\chi N)_{ODT} = 12.399, 9.970,$ and 7.654 , respectively. Unfortunately, the strong polydispersity dependence of $(\chi N)_{ODT}$ still remains, and presumably the same will be true for diblock copolymers with only one polydisperse block.

One possible reason for the apparent failure of the Fredrickson-Helfand treatment is that it becomes inaccurate for small \bar{N} . In the Lynd-Hillmyer experiments, $\bar{N} \approx 1200$ for the poly(styrene)-poly(isoprene) diblocks and $\bar{N} \approx 300$ for the poly(ethylene-alt-propylene)-poly(DL-lactide) diblocks. In our simulations, $\bar{N} \approx 100$ [24]. However, Fredrickson and Helfand [7] state that the approximations involved in their calculation are strictly valid only for $\bar{N} \gtrsim 10^{10}$, conditions for which the ODT is just slightly discontinuous. They do note that the calculation, nevertheless, seems to produce sensible predictions down to $\bar{N} \sim 10^4$, but even this is well above the values characteristic of the experiments and simulations. Not only that, there have been issues raised regarding the validity of the Fredrickson-Helfand theory. Although this has motivated a more rigorous treatment [23], the new method does not yet provide a means of predicting the ODT. The real challenge will be to cope with realistic values of \bar{N} [30], where the A- and B-blocks are already well segregated by the time the ODT occurs. Under such circumstances, the irregular shaped domains of the disordered phase will create a considerable amount of packing frustration [31], which in turn will suppress fluctuations and help induce the ODT. Since packing frustration is alleviated by polydispersity [20], it follows that fluctuations should be amplified at higher PDI_A counteracting the reduction in $(\chi N)_{ODT}$

predicted by SCFT. In fact, this mechanism is effectively the same as Lynd and Hillmyer [15] previously proposed to explain the discrepancy between their results and SCFT.

Of course, we would hope that our Monte Carlo simulations not only corrected the qualitative inconsistency between SCFT and experiment, but also maintained the agreement that has so far been achieved regarding other behaviors. Fortunately, this seems to be the case. The peaks in the disordered-state structure function (see Fig. 9 and Tab. 2) and the periods of the ordered lamellar morphology (see Tab. 3) demonstrate that polydispersity creates a preference for larger domains, which is consistent with both SCFT [17–19] and experiment [13,14,21]. Furthermore, the shift in the order-order phase boundaries towards higher f , established by experiment [14–16] and predicted by SCFT [18–20], is consistent with the transformation of our ordered phase from L to PL. Note, however, that the shift we observe is somewhat stronger than in the Lynd-Hillmyer experiments, where the ordered phase at symmetric composition (*i.e.*, $f \approx 0.5$) remained L up to $\text{PDI}_A = 2.0$.

We must be careful not to assume that the PL phase in our simulations is the true equilibrium phase at large PDI_A . Experiments often observe the PL phase in monodisperse melts, but it generally converts to the gyroid (G) phase given sufficient time [3], which is consistent with the SCFT prediction that PL is slightly less stable than G [32]. In simulations, however, PL is unlikely to convert to G in any reasonable time scale, given how long it can take for defects to anneal out of the L phase. Furthermore, there is the added complication that G has a relatively large cubic unit cell, which has difficulty fitting into finite-sized simulation boxes [9]. Thus when PL was observed in previous Monte Carlo simulations on monodisperse melts, it was just assumed to be a metastable state [8]. The exact same issues reemerge with polydisperse melts. Although experiments observe PL [15,33], it may only be metastable with respect to G, as again suggested by SCFT [20]. Similarly, we suspect that the PL phase observed in our simulations is again a metastable state that forms in place of the G phase, because of its simpler structure and the fact that it fits into the simulation boxes more easily.

The last issue we need to consider involves two-phase coexistence regions, which must in principle separate all single-phase regions [20]. In other words, the transformation from L to a complex phase (*i.e.*, PL or G) with increasing PDI_A will pass through a coexistence region. From previous SCFT calculations [20] and the lack of experimental observations of coexistence, we expect these regions to be relatively narrow near the ODT. Nevertheless, they would be impossible to detect with our simulations, because the simulation boxes are far too small for coexistence to occur. The boxes would have to be large enough that the interfacial tension between the two coexisting phases was negligible relative to their bulk free energies. Coexistence could technically be detected by performing the simulation in the grand-canonical ensemble, but this would be unreasonably complicated because there would have to be a separate chemical potential for each

value of N_A [34]. For now, SCFT [20] seems to be the only practical method of investigating macrophase separation.

6 Conclusions

This study has investigated polydisperse diblock copolymer melts using lattice-based Monte Carlo simulations. Our focus was on melts of symmetric composition (*i.e.*, $f = 0.5$), where the A-blocks were polydisperse with an average of $(N_A)_n = 15$ monomers and the B-blocks were monodisperse each with exactly $N_B = 15$ monomers. The molecular weights of the A-blocks were chosen according to the standard Schultz-Zimm distribution (Eq. (5)) with polydispersity indices ranging from $\text{PDI}_A = 1.0$ (monodisperse) to 2.0 (the most probable distribution). Consistent with previously established behavior, we found that the domain size increases monotonically with PDI_A . We also found evidence for a compositional shift in the order-order phase boundaries by the fact that the L phase switches to the PL phase as PDI_A approaches 2.0. Note that the true equilibrium phase at large polydispersity is very likely G rather than PL.

Our most important finding is that the position of the ODT remains approximately constant for the whole range, $\text{PDI}_A = 1.0\text{--}2.0$, which is consistent with the experiments on poly(ethylene-*alt*-propylene)-poly(DL-lactide) diblocks by Lynd and Hillmyer [15]. This is in stark contrast to the 28% reduction in $(\chi N)_{ODT}$ predicted by SCFT [20], inferring that fluctuation effects are significantly amplified by polydispersity, contrary to what is suggested by the standard Fredrickson-Helfand fluctuation theory [22]. The enhanced fluctuation effects are likely caused by a reduction in packing frustration within the domains formed by the polydisperse blocks.

We are grateful to Christian Burger for supplying us with the fluctuation corrections in reference [22], and we acknowledge the EPSRC (EP/E010342/1) for financial support.

Appendix A. SCFT disordered-state structure function

The disordered-state structure function, $S(q)$, for SCFT has been calculated analytically in references [18] and [19], but in both cases the final result contains typographical mistakes. The corrected expression is

$$S(q) = \left[\frac{S_{AA} + S_{BB} + 2S_{AB}}{N(S_{AA}S_{BB} - S_{AB}^2)} - 2\chi \right]^{-1}, \quad (\text{A.1})$$

where

$$S_{AA} = \frac{2N}{x^2} \left[(1 + fx/k)^{-k} + fx - 1 \right], \quad (\text{A.2})$$

$$S_{BB} = \frac{2N}{x^2} \left[\exp(-(1-f)x) + (1-f)x - 1 \right], \quad (\text{A.3})$$

$$S_{AB} = \frac{N}{x^2} \left[(1 + fx/k)^{-k} - 1 \right] \times \left[\exp(-(1-f)x) - 1 \right], \quad (\text{A.4})$$

and $x \equiv q^2 N a^2 / 6$. Note again that this χ for the Gaussian chain model is slightly different than that for our lattice model in equation (1). Also note that the statistical segment length of our freely jointed chains is $a \approx 1.17b$ [24].

References

1. D.A. Hajduk, P.E. Harper, S.M. Gruner, C.C. Honeker, G. Kim, E.L. Thomas, L.J. Fetters, *Macromolecules* **27**, 4063 (1994); M.F. Schulz, F.S. Bates, K. Almdal, K. Mortensen, *Phys. Rev. Lett.* **73**, 86 (1994).
2. I.W. Hamley, K.A. Koppi, J.H. Rosedale, F.S. Bates, K. Almdal, K. Mortensen, *Macromolecules* **26**, 5959 (1993).
3. D.A. Hajduk, H. Takenouchi, M.A. Hillmyer, F.S. Bates, M.E. Vigild, K. Almdal, *Macromolecules* **30**, 3788 (1997).
4. M. Takenaka, T. Wakada, S. Akasaka, S. Nishitsuji, K. Saijo, H. Shimizu, M.I. Kim, H. Hasegawa, *Macromolecules* **40**, 4399 (2007).
5. M.W. Matsen, M. Schick, *Phys. Rev. Lett.* **72**, 2660 (1994).
6. C.A. Tyler, D.C. Morse, *Phys. Rev. Lett.* **94**, 208302 (2005).
7. G.H. Fredrickson, E. Helfand, *J. Chem. Phys.* **87**, 697 (1987).
8. M.W. Matsen, G.H. Griffiths, R.A. Wickham, O.N. Vassiliev, *J. Chem. Phys.* **124**, 024904 (2006).
9. F. Martínez-Veracoechea, F.A. Escobedo, *Macromolecules* **38**, 8522 (2005).
10. B. Miao, R.A. Wickham, *J. Chem. Phys.* **128**, 054902 (2008).
11. M.A. Hillmyer, *J. Polym. Sci., Part B* **45**, 3249 (2007).
12. D. Bendejacq, V. Ponsinet, M. Joanicot, Y.-L. Loo, R.A. Register, *Macromolecules* **35**, 6645 (2002).
13. N.A. Lynd, B.D. Hamilton, M.A. Hillmyer, *J. Polym. Sci. Part B* **45**, 3386 (2007); the two macrophase-separated samples are consistent with L+C coexistence (private communication).
14. N.A. Lynd, M.A. Hillmyer, *Macromolecules* **38**, 8803 (2005).
15. N.A. Lynd, M.A. Hillmyer, *Macromolecules* **40**, 8050 (2007).
16. A.-V. Ruzette, S. Tencé-Girault, L. Leibler, F. Chauvin, D. Bertin, O. Guerret, P. Gérard, *Macromolecules* **39**, 5804 (2006).
17. M.W. Matsen, *Eur. Phys. J. E* **21**, 199 (2006).
18. S.W. Sides, G.H. Fredrickson, *J. Chem. Phys.* **121**, 4974 (2004).
19. D.M. Cooke, A.-C. Shi, *Macromolecules* **39**, 6661 (2006).
20. M.W. Matsen, *Phys. Rev. Lett.* **99**, 148304 (2007).
21. Y. Matsushita, A. Noro, M. Iinuma, J. Suzuki, H. Ohtani, A. Takano, *Macromolecules* **36**, 8074 (2003); A. Noro, M. Iinuma, J. Suzuki, A. Takano, Y. Matsushita, *Macromolecules* **37**, 3804 (2004).
22. C. Burger, W. Ruland, A.N. Semenov, *Macromolecules* **23**, 3339 (1990); **24**, 816 (1991).
23. P. Grzywacz, J. Qin, D.C. Morse, *Phys. Rev. E* **76**, 061802 (2007).
24. O.N. Vassiliev, M.W. Matsen, *J. Chem. Phys.* **118**, 7700 (2003).
25. U. Micka, K. Binder, *Macromol. Theory Simul.* **4**, 419 (1995).
26. N.A. Lynd, M.A. Hillmyer, M.W. Matsen, *Macromolecules* **41**, 4531 (2008).
27. G.V.Z. Schultz, *Z. Phys. Chem. (Munich)* **B43**, 25 (1939); B.H. Zimm, *J. Chem. Phys.* **16**, 1099 (1948).
28. T. Pakula, K. Karatasos, S.H. Anastasiadis, G. Fytas, *Macromolecules* **30**, 8463 (1997).
29. J.-L. Barrat, G.H. Fredrickson, *J. Chem. Phys.* **95**, 1281 (1991).
30. F.S. Bates, M.F. Schulz, A.K. Khandpur, S. Förster, J.H. Rosedale, K. Almdal, K. Mortensen, *Faraday Discuss.* **98**, 7 (1994).
31. M.W. Matsen, F.S. Bates, *Macromolecules* **29**, 7641 (1996).
32. M.W. Matsen, *J. Phys.: Condens. Matter* **14**, R21 (2002).
33. J. Listak, W. Jakubowski, L. Mueller, A. Plichta, K. Matyjaszewski, M.R. Bockstaller, *Macromolecules* **41**, 5919 (2008).
34. M. Buzzacchi, P. Sollich, N.B. Wilding, M. Müller, *Phys. Rev. E* **73**, 046110 (2006).